Microporous and Mesoporous Materials 360 (2023) 112717

Contents lists available at ScienceDirect

Microporous and Mesoporous Materials

journal homepage: www.elsevier.com/locate/micromeso

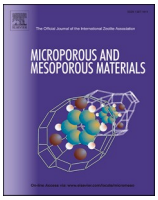

Relationship between multiscale nanopore structure and coal connectivity during coalification process

Zhen Shen [a,*], Zhaoping Meng [a,**], Yu Liu [a], Junhuan Lei [a], Weijun Shen [b], Huaxin Ren [a], Tengwei Gao [a], Kun Zhang [c], Yuheng Wang [a], Libo Tan [a]

[a] College of Geosciences and Surveying Engineering, China University of Mining and Technology (Beijing), Beijing, 100083, China
[b] Key Laboratory for Mechanics in Fluid Solid Coupling Systems, Institute of Mechanics, Chinese Academy of Sciences, Beijing, 100190, China
[c] School of Resources & Environment, Henan Polytechnic University, Jiaozuo, 454000, China

ARTICLE INFO

Keywords:
Pore size
Permeability
Volume
Porosity
Coalification

ABSTRACT

The complex nanopore structures in coal provide the space for gas adsorption and migration, which is crucial for the development of coalbed methane. However, the mechanism of the evolution of multi-scale nanopore structures during coalification is still unclear. In this work, a combined method of CO_2/N_2 adsorption and synchrotron radiation Nano-CT experiments were used to reveal the multi-scale pore structure characterization during coalification. The synchrotron radiation Nano-CT experiment reconstructed the 3D pore network model for different rank coal and revealed the effective diameter is less than 0.5 μm, accounting for 97.4%–99.6% of the total number of macropores. The combination of these methods, including CO_2/N_2 adsorption and Nano-CT, accurately characterizes the multi-scale pore distribution in coal, ranging from <2 nm, 2–300 nm and 64 nm - 3.5 μm. The ultra-micropores occupy the primary advantage, accounting for approximately 60.3%–95.2% of the total pore volume and the micropores, mesopores and macropores are more poorly developed than ultra-micropores. During the coalification process, the proportion of porosity contributed by ultra-micropores to the total porosity gradually increases, with the contribution rising by 57.9%. The proportion of porosity contributed by micropores, mesopores and macropores to the total porosity gradually decreases, with the contribution decreasing by 81.0%, 82.8% and 93.6%, respectively. Besides, with growing coal maturity, the total permeability gradually decreases by 9.26×10^{-3} - 3.05×10^{-1} mD, which is negatively correlated with coal maturity during coalification. And the total permeability is mainly provided by macropores, which account for about 99% of the total permeability. This research provides an in-depth understanding of the storage and transport of coalbed methane in a multi-scale nanopore structure.

1. Introduction

The consumption of traditional fossil fuels, resulting in increased worldwide environmental pollution. As a result, the development of clean energy resources, particularly coalbed methane (CBM) in low-permeability reservoirs, has become a research hotspot in the energy field [1–3]. The developed pores and fractures in coal are the space where the methane is stored and migrated [4–6]. Owing to the alters in the sedimentary environment, the pores and fractures were compacted or filled during coalification, reducing the seepage capacity of the coal. This limits the development of clean energy from coalbed methane in low-permeability coal reservoirs and creates a threat of gas outbursts [7, 8]. Therefore, the mechanism of the multiscale pore and permeability evolution of coal reservoirs during coalification is considered by scholars as an urgent problem that needs to be solved [9–12].

Nanoscale pores are well developed in coal reservoirs, with pore sizes less than 10 nm, which provides enough space for methane adsorption, desorption and seepage. And they play a bridge role to connect large pores and form a pore network system [13–15]. The advanced technology, including image characterization and fluid invasion methods, can be widely used to study the morphology and physical properties of pores in coal reservoirs [16–19]. The display of the pore geometry morphology in the coal can be achieved by scanning technology to obtain 2D information about the pores [20–22]. Such as scanning

* Corresponding author.
** Corresponding author.
E-mail addresses: shenzhen@student.cumtb.edu.cn (Z. Shen), mzp@cumtb.edu.cn (Z. Meng).

https://doi.org/10.1016/j.micromeso.2023.112717
Received 21 March 2023; Received in revised form 7 June 2023; Accepted 26 June 2023
Available online 3 July 2023

transmission electron microscopy (TEM), electron microscopy (SEM), focused ion beam-SEM (FIB-SEM) and atomic force microscopy (ATM). In addition, the morphology of pores in 3D space can be investigated by Micro-/Nanofocus X-ray computed tomography (Micro-/Nano-CT) to determine the physical properties of pores (e.g. pore size, volume, porosity, connectively) [22–25]. Although these methods can directly observe the morphology and structure of pores without damaging them, the limited resolution doesn't provide real information about full-scale pore sizes or distribution characteristics. The fluid invasion methods have been widely used to investigate the nanopore structures by gas adsorption (e.g.CO_2/N_2) and mercury intrusion porosimetry (MIP), which can provide the pore size distribution, volume and connective, etc. In general, the pore size determined by CO_2 adsorption is less than 2 nm, the low-pressure nitrogen adsorption can be used to obtain the pore size distribution of 2–200 nm, and the pore sizes ranging from nanometers to micrometers was effectively characterized by MIP [26–29]. Besides, owing to the Ar or Kr at 77 K isothermal, a more accurate determination of the BET surface area and the pore size distribution of the ultra-micropores can be obtained, which is widely used to determine the characteristics of porous media [30]. Based on the gas adsorption data, the Pore Size Distribution (PSD), Specific Surface Area (SSA) and Pore Volume (PV) can be obtained by the classical density functional theory (DFT), Brunauer-Emmett-Teller (BET) and the Barret-Joyner-Halenda (BJH) theory model, etc. Notably, the non-local DFT (NLDFT) and quenched solid DFT (QSDFT) are commonly used to determine the pore size distribution of porous media [31–34]. The above study reveals the characteristics of nanoscale pore structure in coal, but the fluid invasion methods may cause pore closure or collapse. It is also impossible to achieve the visualization of pore structures in 3D space. Therefore, the multi-scale pore structure characterized in coal cannot be tested by a single method, and it should be applied a combination of technologies to overcome the limitations.

Pore connectivity in coal reservoirs controls the fluid diffusion and seepage capacity, and the gas transport process was also affected [35]. Previous studies found that the fluid intrusion test can be an effective assessment of pore connectivity in coal [36–38]. While there are many well-developed micropores in coal, the molecular probe cannot penetrate into the pore space, resulting in unreliable pore connectivity. In addition, the accuracy of the connectivity of the micro-fractures as measured by the liquid intrusion is less than the direct observation techniques (e.g. Micro-/Nano-CT, FIB-SEM) [22–25]. For example, the 3D pore network model can be reconstructed by CT scanning to investigate pore connectivity. But it should be noted that due to the limited resolution of CT scanning, the small pores developed in the coal may not be detected, which will cause errors in calculation permeability [39].

In this paper, a combined method of CO_2/N_2 adsorption and synchrotron radiation Nano-CT experiments were used to investigate the full-scale pore structure characterization during coalification. The objectives of this study are as follows: (1) the 3D pore network model is reconstructed by synchrotron radiation Nano-CT experimental to clarify the evolution in the number of pore sizes in coal during coalification; (2) determine the pore volume, porosity and initial permeability in the multi-scale pore interval. This work will improve understanding of the evolution mechanism of nanoscale pores during coalification and guide the development of CBM in low-permeability seams.

2. Samples and experimental methods

2.1. Coal samples

Deposited under different sedimentary environments, due to the metamorphism of coal, coal can be divided into high-($R_{o,\ max} > 2.0\%$), medium- ($R_{o,\ max} = 0.65\%–2.0\%$), and low-rank coals ($R_{o,\ max} < 0.65\%$) [19] (ISO 22760-2005). For this experiment, a total of four coal samples were collected from Sihe (S–H, $R_{o,\ max} = 2.91\%$) and Zhaozhuang (Z-Z, $R_{o,\ max} = 2.16\%$) coal mine in Qinshui Basin, Shoushan (S–S, $R_{o,\ max} = 1.31\%$) coal mine in Henan Province and Xianfeng (X–F, $R_{o,\ max} = 0.42\%$) coal mine in Yunnan Province, China. To remove the moisture, all coal samples were crushed and put in a vacuum drying oven to dry the coal samples at 378.15 K for 24 h. Then, the coal samples were analyzed by N_2 adsorption, CO_2 adsorption, and synchrotron radiation Nano-CT. The petrographical results of porosity, maximum vitrinite reflectance ($R_{o,\ max}$, %), coal composition, and proximate analysis are listed in Table 1.

2.2. Experimental methods

2.2.1. Low-pressure N_2 (LP-N_2-GA) and CO_2 (LP–CO_2–GA) adsorption experiment

The LP-N_2-GA and LP–CO_2–GA experiment was conducted by a Nova 2000e Surface Area Analyzer and Pore Size Analyzer (Quantachrome Instruments), following the GB/T19587–2004 standard. The samples were pulverized to 60–80 mesh powder for N_2 adsorption. The container temperature was kept at 77.3 K during the N_2 adsorption experiment. The density functional theory (DFT), Brunauer-Emmett-Teller (BET) [31,32] and the Barret-Joyner-Halenda (BJH) theory model has been proven to an effective method to measure the Pore Size Distribution (PSD), Specific Surface Area (SSA) and Pore Volume (PV) of mesopores, respectively.

For the LP–CO_2–GA experiment, the samples also were pulverized to 60–80 mesh powder. The container temperature was kept at 273.15 K during the CO_2 adsorption experiment. The density functional theory (DFT) and Dubinin-Astakhov (DA) methods were used to obtain the PSD, SSA, and PV of micropores, respectively [33].

2.2.2. Synchrotron radiation Nano-CT

Nano-CT is a method for obtaining 2D images by synchrotron X-ray beam based on the different densities of materials and employs computer image reconstruction technology to construct high-resolution 3D images. The synchrotron radiation Nano-CT was employed at the 4W1A beamline of Beijing Synchrotron Radiation Facility (BSRF) in this study, which has a stable synchrotron X-ray energy (5–12 keV) and a high-resolution of 30 nm for Nano-CT scanning [23,40]. From Fig. 1, the sample on the turntable rotates discontinuously for well-defined angular intervals to capture images at different angles during Nano-CT scanning. Simultaneously, it takes 30 s to obtain a single 2D image by the CCD camera and the data is transmitted to the computer to reconstruct the 3D image.

Before synchrotron radiation Nano-CT, the sample was pulverized to 40–60 mesh particles and was stuck on the tip of the pin with a microscope. Then, the pin was fixed on the turntable and a gold particle was plated on the sample by using the magnifier instrument when the experiment began, as shown in Fig. 2. In this experiment, there are 1024 two-dimension images were collected for each sample, in which each voxel pixel size was approximately 0.064 × 0.064 μm. These 2D images were imported into Avizo software to reconstruct the 3D spatial volume based on the fast watershed algorithm [41]. Based on different densities, threshold segmentation was used to accurately identify the matrix, pores/fractures, and minerals in 3D reconstruction. Owing to the raw sample being irregular, it requires random selection of a region of interest (ROI) as the study object and quantitative analysis of the pore distribution characteristics in the internal structure of the sample (Fig. 2-E). The reconstructed sub-volume of each coal sample was 19.2 × 19.2 × 19.2 μm^3 and the size of ROI was 300 × 300 × 300 voxels.

2.2.3. Porosity calculation

Porosity is a key parameter to characterize the development of pore structure in coal. Based on synchrotron radiation Nano-CT scanning, the pore volume was calculated by Avzio software, and the mass of the coal 3D dataset was obtained by Eq. (1) and Eq. (2) [39,42]. The porosity of every coal sample was calculated as the following formula Eq. (3) [43].

Table 1
Proximate analysis and petrographical data of coals.

Sample	$R_{o,\ max}$ (%)	Coal composition				Proximate analysis			Density (g/cm^3)	Φ (%)
		V (%)	I (%)	E (%)	M (%)	M_{ad} (%)	A_{ad} (%)	V_{ad} (%)		
S–H	2.91	94.30	0.47	0	5.23	1.92	8.62	6.25	1.42	10.1
Z-Z	2.16	87.92	5.94	0	6.14	0.89	10.63	10.68	1.37	7.5
S–S	1.31	74.40	22.70	0	2.90	0.82	12.97	24.52	1.30	4.5
X–F	0.42	80.20	17.80	0.50	1.50	29.56	5.45	35.60	1.18	4.7

Note: V- vitrinite, I- inertinite, E−exinite, M − mineral, M_{ad}-moisture A_{ad}-ash, V_{ad}-volatile matter, density-bulk density, and Φ-total porosity.

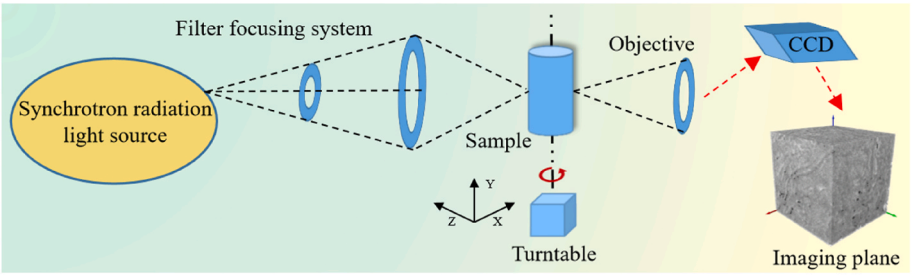

Fig. 1. Synchrotron radiation Nano-CT schematic.

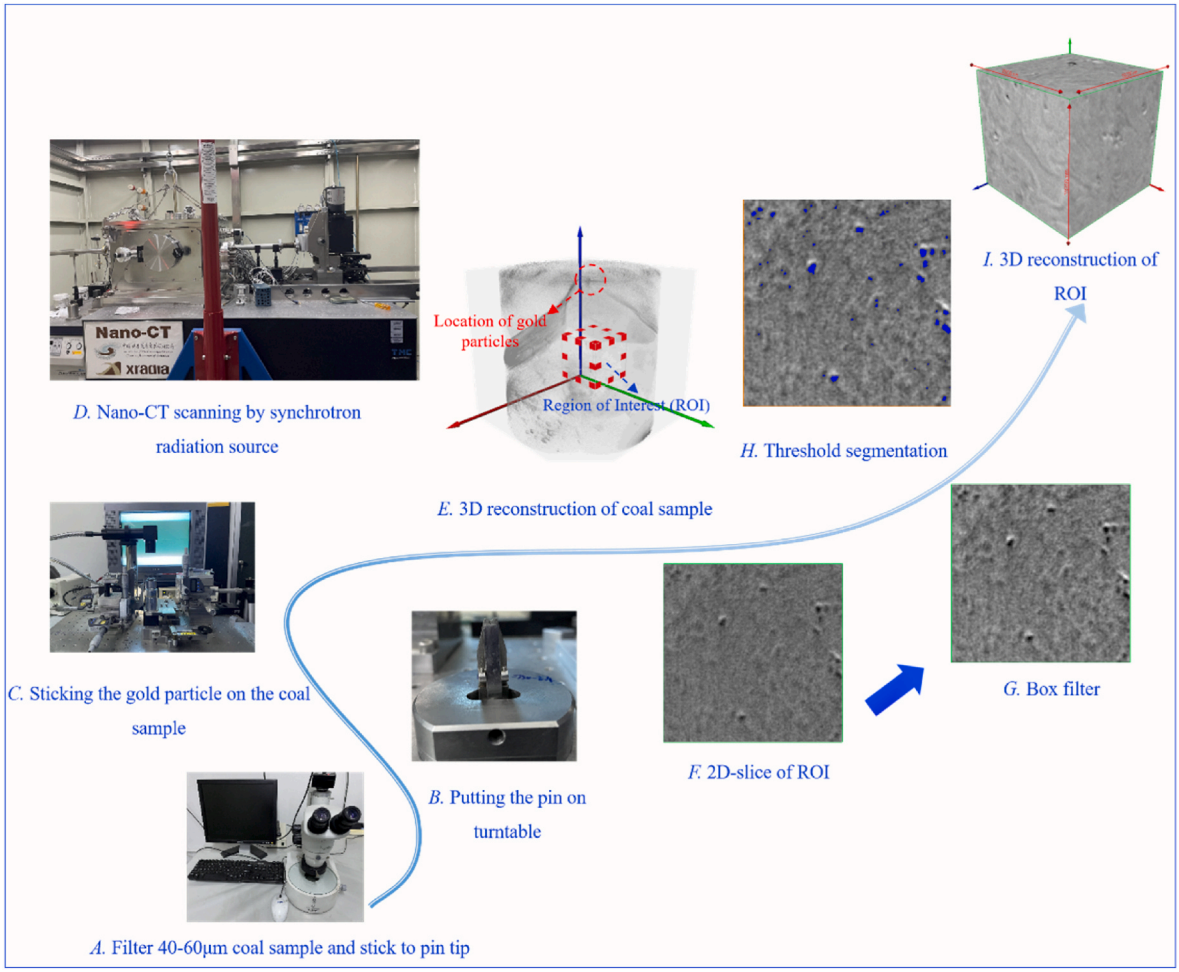

Fig. 2. Synchrotron radiation Nano-CT experiment procedure.

$$M = \rho \bullet V_1 \quad (1)$$

$$V_3 = \frac{V_2}{M} \quad (2)$$

$$\Phi = \frac{V_4}{1/\rho} \bullet 100\% \quad (3)$$

Where M is the 3D reconstructed sub-volume mass of coal in ROI, g; ρ is the density parameter of coal, g/cm^3; V_1 is the sub-volume of the coal, cm^3; V_2 is the pore volume in Nano-CT scanning, cm^3; V_3 is the pore volume of unit mass coal sample, cm^3/g; V_4 is the unit volume for the pore diameter interval, cm^3/g; Φ is the porosity of coal sample, %.

3. Results

3.1. LP-CO_2 -GA adsorption experiment

The isothermal adsorption of CO_2 is an effective method for the study of the micropore structure of coal. From Fig. 3 (a), the sorption capacity of coals from low to high rank is shown by the CO_2 sorption curve, which belongs to the Type I curve according to the classification of IUPAC [44]. The experimental results showed that the CO_2 adsorption of the four coal samples increased with rising relative pressure, as follows the order: high-rank coal (S–H > Z-Z) > median-rank coal (S–S) > low-rank coal (X–F). The cumulative micropore volume with a pore size of 0.3–2 nm, as measured by the DFT model, is 0.068 cm^3/g, 0.048 cm^3/g, 0.027 cm^3/g, and 0.024 cm^3/g, respectively. Especially, the micropore volumes in the high-rank coal are greater than other rank coals, implying that micropores are well developed in the high-rank coal. The pore size distribution (PSD) curve of various rank coals is plotted in Fig. 3 (b). The multiple peak values of PSD can be divided into three stages: 0.4–0.6 nm, 0.6–0.7 nm, and 0.7–0.9 nm, respectively. Remarkably, the high-rank coal sample (S–H) has a peak value in the 0.3–0.4 nm pore size range, which indicates that the pores gradually condense into smaller micropores as the degree of metamorphism increases. For medium- and low-rank coals, the pore sizes are mainly concentrated in the 0.6–0.7 nm and 0.7–0.9 nm ranges, with a smaller peak value than the high-rank coals.

3.2. Pore structure from LP-N_2-GA adsorption experiment

The LP-N_2-GA adsorption/desorption experiment results in various rank coals were showed in Fig. 4. They have markedly different morphologies observed in N_2 adsorption/desorption curve from four coal samples, which belong to the type IV isotherm and H_3 hysteresis loops by the IUPAC classification [45]. From the shape of the N_2 adsorption/-desorption curve, the adsorption capacity of N_2 in coal samples increases slowly and the adsorption/desorption curves are basically consistent ($P/P_0 < 0.5$). This phenomenon is caused by the gas adsorption in a monolayer on the porous surface, which implies that the connectivity of the micropores in coal samples is poor. It can also be observed that the adsorption capacity of median-rank coal (S–S sample) is greater than low-rank coal (X–F sample), indicating that the proportion of micropores increases with growing coal maturity. In contrary, the adsorption capacity of high-rank coal (S–H and Z-Z sample) is less than median-rank coal, implying that the connectivity of the micropores in high-rank coals is relatively poor. Moreover, owing to the coal being a porous medium with strong heterogeneity, the N_2-multilayer coverage will cause an obvious hysteresis loop ($P/P_0 > 0.5$) [46]. And capillary condensation will appear during this process, which promotes the obvious increase of N_2 adsorption capacity. It is noted that the hysteresis loop of medium-rank coal is the most obvious. This phenomenon indicates the existence of tiny or ink-bottle shaped pores with good connectivity in the coal. In summary, there are continuous and open pore system exit in coal samples (e.g. slit-shaped pores, ink bottle-shaped pores and cylindrical pores) [19,45]. The PSD range of various rank coals was obtained from 3 nm to 350 nm by N_2 adsorption, as shown in Fig. 4 (b). It is observed that pore volume first increases and then decreases as pore size increases. When the pore size is 2–4 nm, the pore volume tends to increase and gradually reaches a peak value. However, above the 4 nm pore size, the pore volume decreases sharply. Besides, with the increase in coal maturity, the pore volume also decreases significantly. And the cumulative volume of various rank coals is 2.485×10^{-2} cm^3/g, 2.072×10^{-2} cm^2/g, 2.753×10^{-2} cm^3/g and 6.834×10^{-2} cm^3/g, respectively. Compared with median- and high-rank coal, the cumulative volume of low-rank coal is approximately twice that of them. The results imply that the development of micropores in coal is better than mesopores and macropores. Moreover, pores in low-rank coal are well developed than the median- and high-rank coal.

3.3. Pore morphology and structure from synchrotron radiation Nano-CT experiment

Based on the grayscale, the two-dimensional slices of different rank coals can be obtained by the synchrotron radiation Nano-CT experiment, as shown in Fig. 5 (a). The mineral is a light gray color with the high-density, the medium-density parts have a dark gray color, which represents the coal matrix and the lowest-density is marked by black gray color, which represents the pores (pores were marked in blue color during threshold segmentation) [40]. It is observed that the pore morphology in coals is mainly wedge-shaped pores, cylindrical-shaped pores and parallel plate-shaped pores. As the maturity (metamorphism) of the coal increases, the number of pores on the surface of the coal decreases. Moreover, several parallel plate-shaped pores will appear on the surface of the median- and high-rank coals. For example, there are many pores on the surface of two-dimensional slices of low-rank coal (Fig. 5, g-h). In contrast, the number of pores produced on

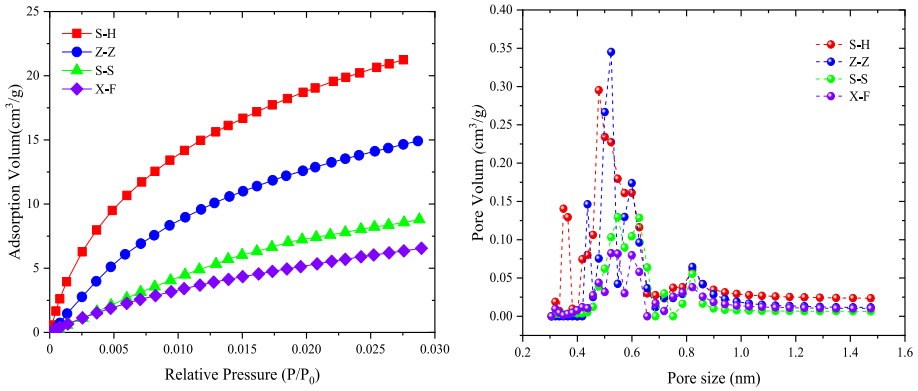

Fig. 3. (a) CO_2 adsorption curves at various rank coals; (b) Structure of 0.3–2 nm pore volumes distribution obtained by CO_2 adsorption.

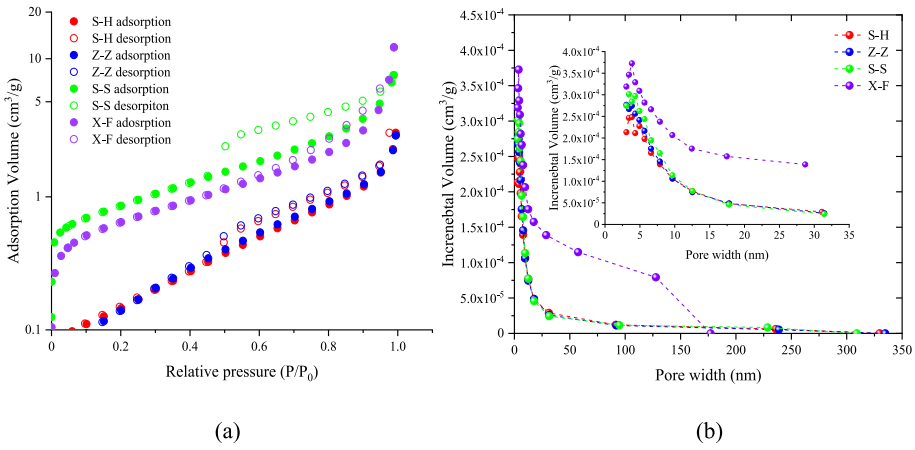

Fig. 4. (a) Low-pressure N_2 adsorption/desorption experiment data in coal samples; (b) Pore size distribution obtained by N_2 adsorption.

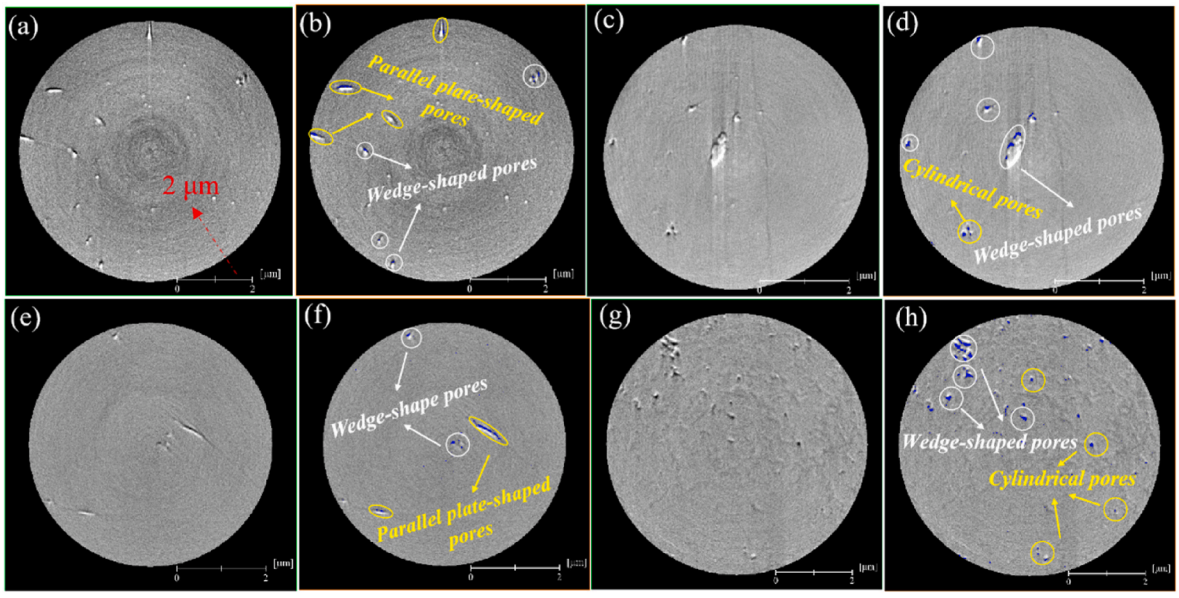

Fig. 5. Two-dimensional pore morphology characteristics of different rank coals.

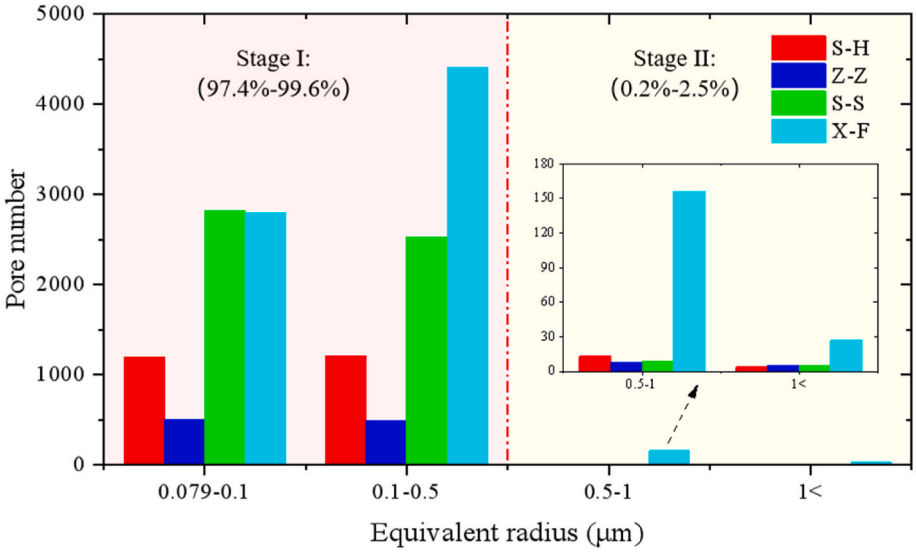

Fig. 6. Quantitative analysis of the pore number in different rank coals by using synchrotron radiation Nano-CT scanning.

the surface of medium- and high-rank coals are small, with the formation of parallel plate-shaped pores (Fig. 5, a-b, c-d, e-f). This is a phenomenon caused by coal metamorphism. Owing to the change in temperature and pressure, the low-rank coal is transformed into medium- and high-rank coals, during which pores are condensed and gradually reduced [23,41]. On the contrary, there will be an increase in the number of micro- and mesopores in the medium- and high-rank coals (Fig. 3). From Fig. 6, proves this view about the number of pores is gradually reduced, while there will be an increase in the number of micro- and mesopores during the low-rank coal is transformed into the medium- and high-rank coals. The number of pores in different rank coals can be divided into two stages in this study. Stage I, the effective diameter is less than 0.5 μm, and the number of pores will account for approximately 97.4%–99.6% of the total number of pores. Stage II, the effective diameter is greater than 0.5 μm, and the number of pores will account for approximately 0.2%–2.5% of the total number of pores. Besides, the effective pixel of synchrotron radiation Nano-CT is only 0.064 μm, therefore, it can be concluded that pores with an equivalent diameter of 0.064–0.5 μm are developed well in coal follows the order: low-rank coal > median-rank coal > high-rank coal.

3.4. Calculation the pore volumes based on the synchrotron radiation Nano-CT experiment

The Pores development in coal is usually irregular in shape (e.g. ellipsoidal, ink-bottle, slit-shaped pores), which are mostly isolated with poor connectivity. Owing to the gas being stored in the pore, it can't migrate out. As a result, coalbed methane production continues to decline. To reveal the phenomenon, the 3D-reconstruction model of a coal sample was built (Fig. 7). The coal matrix, pore and mineral in the 3D-reconstruction model were masked by red color, yellow color and white color, respectively. Moreover, a detailed representation of the pore distribution in 3D space is provided by the ball-stick model. From Fig. 8, the correlation between the multi-scale pore diameter and the pore volume of the different rank coals is obtained as follows: low-rank coal > median-rank coal > high-rank coal. At the multi-scale pore diameter interval, the pore volume of the low-rank coal is significantly greater than other rank coals. For example, in the mesopores stage (0.079–0.1 μm), the pore volume of low-rank (X–F coal) is 1.051×10^{-4} cm^3/g, but for the median- (S–S coal) and high-rank coals (Z-Z and S–H coal), the pore volume is 1.047×10^{-4} cm^3/g, 1.869×10^{-5} cm^3/g and 4.351×10^{-5} cm^3/g, respectively. For the macro-pores stage (0.1–0.2 μm), the pore volume of low-rank, median-rank and high-rank coals are 5.692×10^{-4} cm^3/g, 3.555×10^{-4} cm^3/g, 6.689×10^{-5} cm^3/g and 1.656×10^{-4} cm^3/g respectively. In addition, as the pore diameter increases, the pore volume of low-rank coal is positively correlated with the pore diameter. This result shows that mesopores and macropores are well-developed in low-rank coal. For the medium-and high-rank coals, the pore volume increases significantly when the pore diameter is greater than 1 μm. The volumes of the other pore diameter intervals are not significantly different.

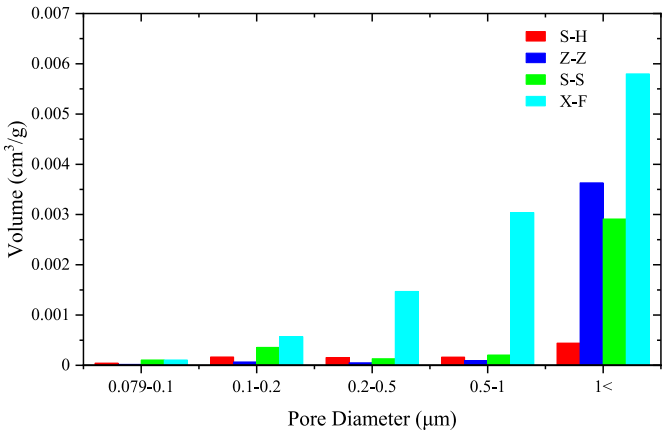

Fig. 8. Pore volumes in multi-scale pore size intervals for different ranked coals.

4. Discussions

4.1. Full-scale pore size distribution characteristics of low-median-high rank coals

Nanopore evolution characteristic is one of the important elements in studying the development of coalbed methane. As metamorphism progresses, low-rank coals transition to medium- and high-rank coals, and pore volumes alter more complex. Therefore, to accurately characterize the multi-scale pore distribution in coal, a combination of these methods, including CO_2/N_2 adsorption and Nano-CT, is required to overcome the limitations of a single technology. According to the pore size classification provided by IUPAC, the pores were divided into micropores (<2 nm), mesopores (2–50 nm), and macropores (>50 nm) [50]. Obviously, it does not apply to this study. Based on the experimental results, we adopted the pore size classification proposed by Zhang et al. [51], who divided the pore size into ultra-micropores (<2 nm), micropores (2–10 nm), mesopores (10–100 nm) and macropores (>100 nm). So, the multi-scale pore size of coal was quantified by CO_2/N_2 adsorption and synchrotron radiation Nano-CT, ranging from <2 nm, 2–300 nm and 64 nm - 3.5 μm, respectively. It should be noted that the pore size range was quantified by synchrotron radiation Nano-CT, including pore size by N_2 adsorption. Owing to N_2 adsorption will promote the expansion of pore volume, in contrast, synchrotron radiation Nano-CT is highly accurate and does not damage pore morphology. So, the overlapping range was determined by synchrotron radiation Nano-CT.

From Fig. 9, it can be observed that the ultra-micropores in various rank coals occupy the primary advantage, accounting for approximately 60.3%–95.2% of the pore volume. The volumes of ultra-micropores from low-rank coal to median- and high-rank coal is 2.401×10^{-2} cm^3/g, 2.748×10^{-2} cm^3/g, 4.783×10^{-2} cm^3/g, 6.799×10^{-2} cm^3/g, respectively. In contrary, the micropores, mesopores and macropores are more poorly developed than in coal, accounting for approximately 0.7%–9.7%, 1.7%–9.9% and 1.3%–20.2%, respectively. For the X–F coal

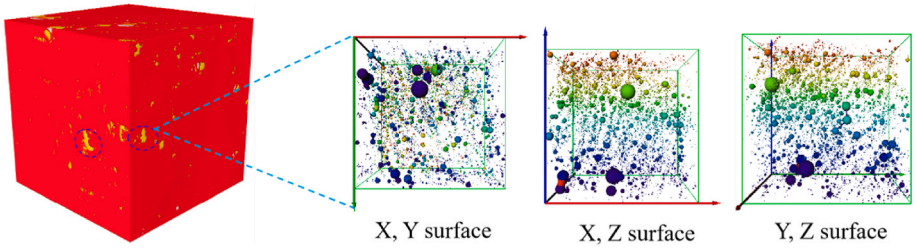

Fig. 7. 3D reconstruction of coal samples by synchrotron radiation Nano-CT scanning.

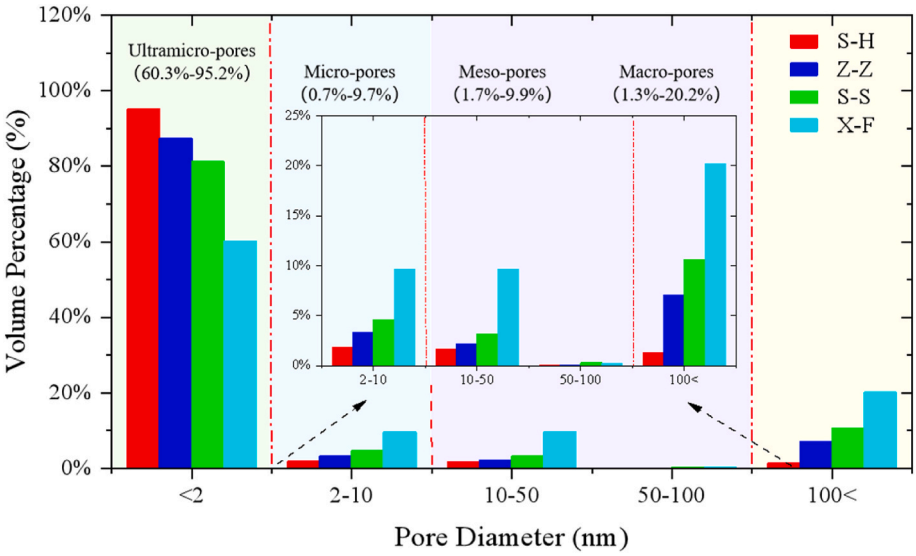

Fig. 9. The full-scale pore volumes percentages of the different rank coals.

sample, the volumes of ultra-micropores, micropores, mesopores and macropores are 2.401×10^{-2} cm^3/g, 3.848×10^{-3} cm^3/g, 3.953×10^{-3} cm^3/g, 8.04×10^{-3} cm^3/g, accounting for 60.3%, 9.7%, 9.9% and 20.2%, respectively. At this stage, a large number of macropores are present in the low-rank coal. With the rise of coal metamorphism, the volumes of full-scale pore diameter intervals have undergone a dramatic alter. The volumes of ultra-micropores increase significantly from low to medium- and high-rank coals by 14.4%, 99.2% and 183.2%, respectively. However, the volumes of micropores, mesopores and macropores are reduced by 8.4%–11.1%, 11.3%–11.5% and 17.5%–29.6%, respectively.

It can also be seen by changing the total pore volume, as shown in Fig. 10. From low to medium- and high-rank coals, the total pore volume initially decreases and increase. These phenomena can be revealed from a microscopic perspective (Fig. 11). In the early stages of coalification (first coalification jump), the coal has a relatively low degree of metamorphism, with long side chains of aliphatic structured in its molecular structure, resulting in a loose molecular space structure (e.g. low-rank coal) [52]. The pore volume in low-rank coal is relatively large. Owing to the rise of temperature and pressure (e.g. median-rank coal), the coal macromolecular structure was influenced by polycondensation during coalification, the bridge bonds broke and aliphatic structures began to drop off in the macromolecular structure of coal, forming small aromatic rings. Therefore, the pore volume of the coal initially decreases

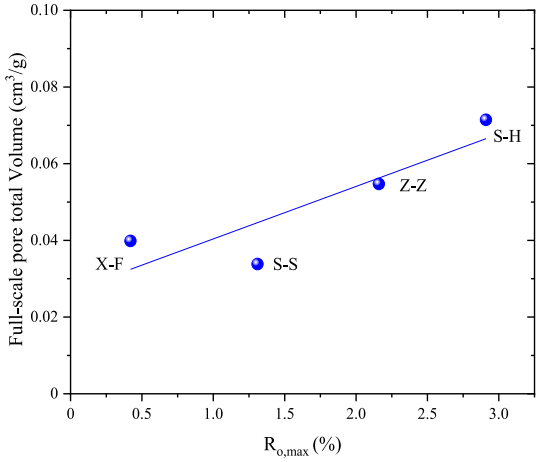

Fig. 10. Variation of total pore volume with $R_{o,\ max}$.

with increasing $R_{o,\ max}$. It should be noted that macropores are more susceptible to physical compaction during the coalification process, which causes a reduction in pore volume as pore size decreases (Fig. 8). In contrast, ultra-micropores (pore size <2 nm) are controlled by coal molecular, and the aliphatic fall off will contribute to an increase in the volume of ultra-micropores. When the coal reaches a stage of maturity (e.g. high-rank coal), the condensation of small aromatic rings forms large aromatic rings, and the large aromatic rings rearrange to form a denser molecular structure. This result implies that the ultra-micropores are well developed in high-rank coal.

4.2. Porosity contribution of different types of pores in various rank coal

In this study, the evolution of porosity in different rank coals was determined by the combined method of CO_2/N_2 adsorption and synchrotron radiation Nano-CT during coalification. According to Eq. (3), the porosity of the pore was calculated by the pore volume and the bulk density of the coal (Table 1). The total porosity of coals can be attained to be 10.1%, 7.5%, 4.5% and 4.7%, respectively. In general, the porosity was measured by the combined method of CO_2/N_2 adsorption and synchrotron radiation Nano-CT differed from the porosity calculated by Helium pycnometry. The reason may be that the molecular probe of CO_2/N_2 cannot penetrate into the smaller pore space and the small pores may also not be detected by the limited resolution of Nano-CT scanning, resulting in different porosity [6,43].

From Fig. 12, it can be observed that as the maturity of the coal increases, the proportion of porosity contributed by different pore types to the total porosity can be divided into two categories. The first is that as the maturity of the coal grows, the proportion of porosity contributed by ultra-micropores to the total porosity gradually increases from 60.2% to 95.2%, with the contribution increasing by 57.9%. And the porosity of the ultra-micropores increases from 2.8% to 9.7%. This phenomenon explains that the number of ultra-micropores is better than other pore sizes with growing maturity. Whereby, it can prove that the volume of ultra-micropores takes up an absolutely dominant in different rank coals (Fig. 9). In contrary, the proportion of porosity contributed by micropores, mesopores and macropores to the total porosity gradually decreases from 9.7% to 1.8%, 9.9% to 1.7% and 20.2%–1.3%, with the contribution decreasing by 81.0%, 82.8% and 93.6%, respectively. Noted that owing to the small porosity of micropores, mesopores and macropores were calculated by Eq. (3), the measured value in the experiment was 0. Therefore, the variation in the porosity of the micropores, mesopores and macropores can be ignored in this manuscript.

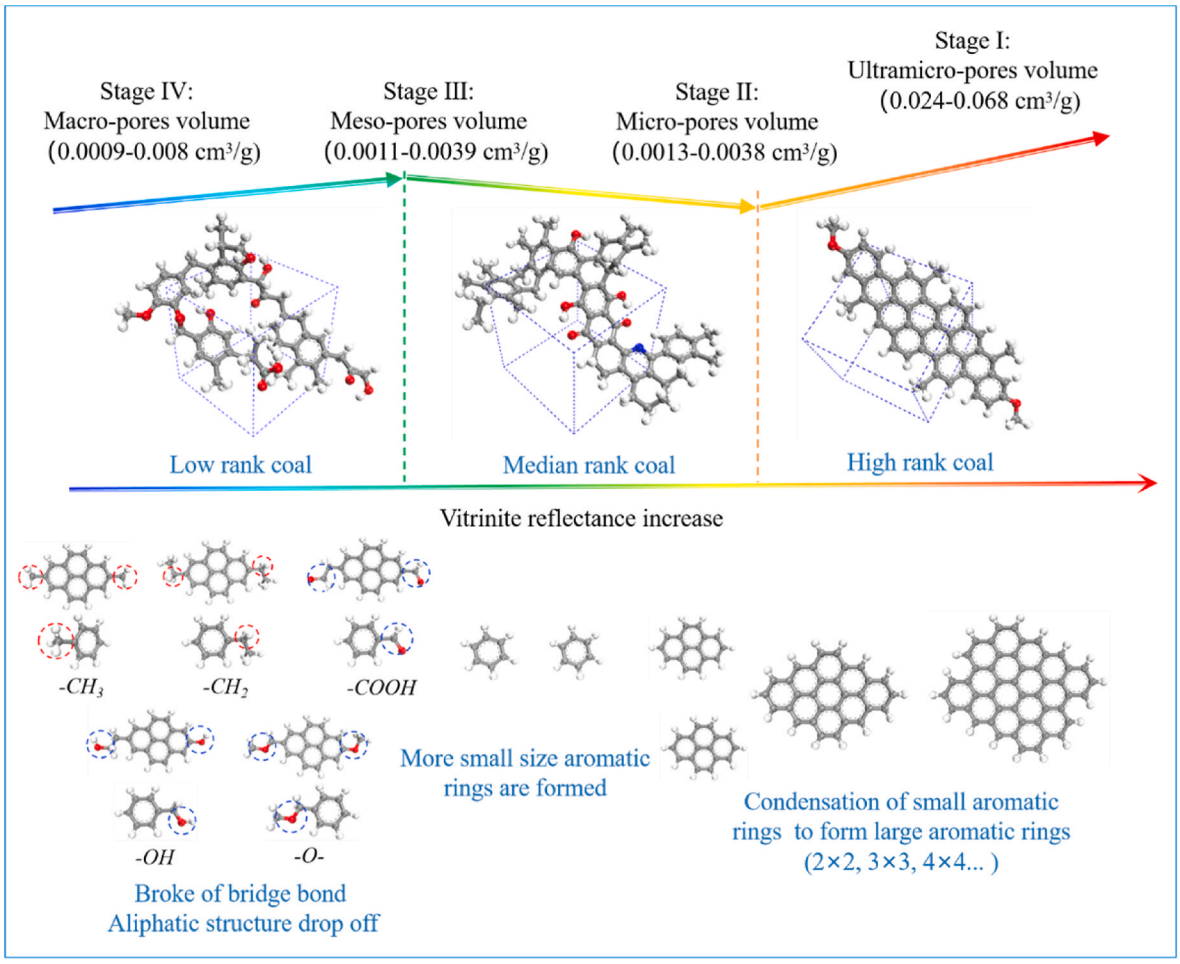

Fig. 11. The mechanism of pore volume evolution during the coalification process.

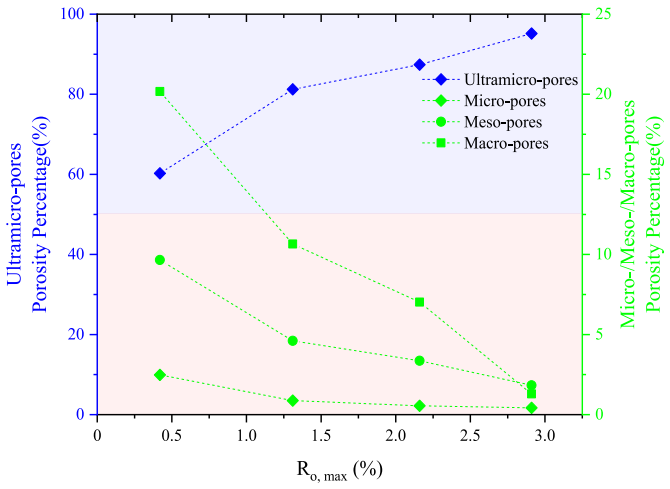

Fig. 12. Proportion of porosity of different pore types in the total porosity.

These results imply that the number of micropores, mesopores and macropores are negatively correlated with the maturity of the coal. The reason may be generated by the altering of temperature and pressure during coalification (Fig. 13). Owing to the variable burial depths, the diverse temperature-pressure conditions in the coal reservoir will cause the coal molecular structure to alter [53]. Whereby, the aliphatic structure is gradually falling off and the order of the molecular structure of the coal is increasing, which will lead to a reduction in the number of pores (Figs. 11 and 13). In addition, it is generally accepted that physical compaction plays an important role in the formation of pores during coalification [43,54]. Therefore, in the process of compaction, the large pores (e.g. macropores) were blocked or filled by asphaltene with cementation, resulting in a rapid decline in porosity. So, it can be seen that the contribution proportion of large pores porosity in the low-rank coal is greater than other rank coals [55]. These results imply that physical compaction tightens the coal reservoir during coalification. Therefore, the contribution of micropores, mesopores and macropores decreases with increasing maturity. Simultaneously, it can be observed that the proportion of porosity contributed by different pore types to the total porosity follows the order: ultra-micropores > micropores > mesopores > macropores. It will become more obvious that there is a difference between other pore types (e.g. micropores, mesopores, macropores) and ultra-micropores with growing maturity. This reason may be that the aromatic structure condensation increases the number of ultra-micropores and greatly improves the contribution of ultra-micropores (Fig. 13). And the dissolution is the main factor controlling the increase in nanoscale pores, contributing to greater porosity [56,57].

4.3. Evolution mechanism of coal reservoir permeability during coalification

The adsorption of methane molecules in coal is extremely complex and large proportions of methane molecules are adsorbed on the surface of pore wall. As the pore size increases, the methane molecules are less affected by pore wall. As a result, the methane molecules break free from

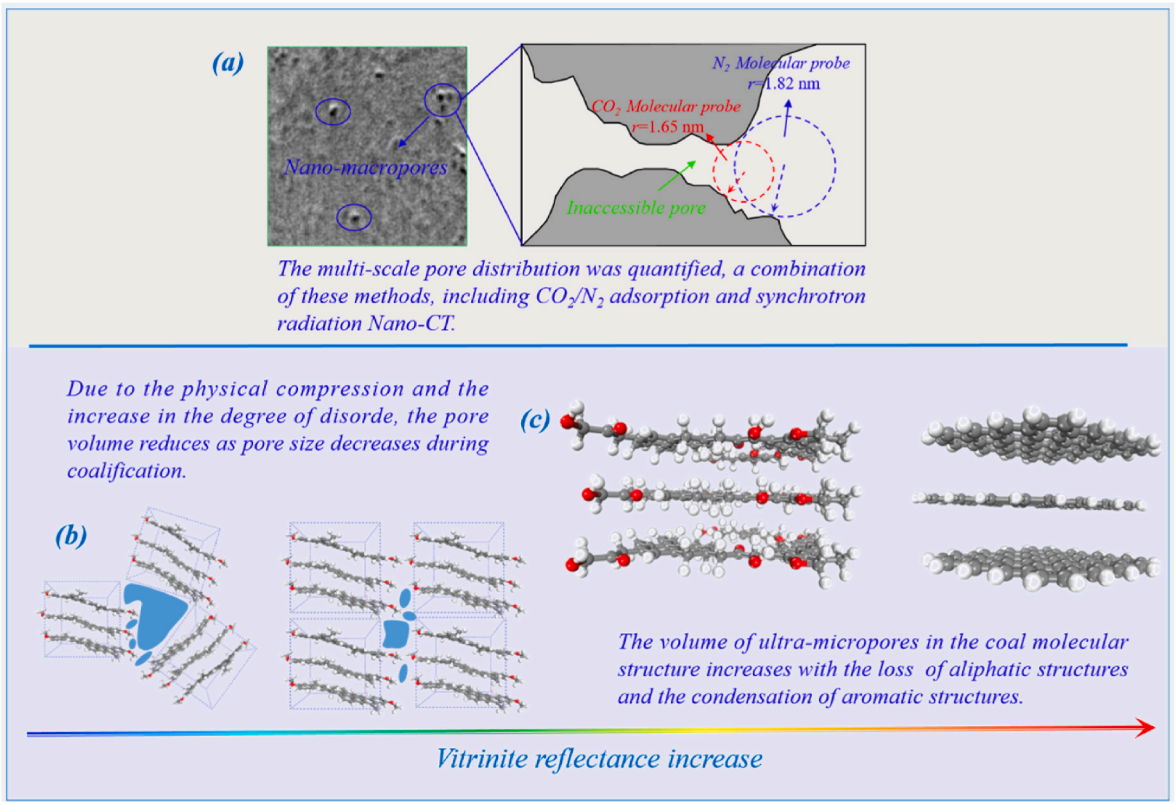

Fig. 13. Porosity evolution process of nanoscale pore.

the pore walls and more methane molecules are stored in the pores of the coal with a free state [58,59]. Therefore, pores in coal reservoirs provide channels for gas migration and they are also important factors in controlling permeability. To reveal the permeability evolution of the nanoscale pore diameter interval, a theoretical model proposed by Carman [33] was used in this paper. In here, the permeability K_1 or K_2 is a capillary bundle under ideal conditions, which can be calculated by combining Darcy's law with the Hagen-Poiseuille equation as follows [35,39]:

$$K_1 = \frac{\Phi\gamma^2}{8\tau^2} \tag{4}$$

$$K_2 = \frac{\Phi r^2}{12\tau^2} \tag{5}$$

$$\tau = \frac{\Phi}{\left[1-(1-\Phi)^{\frac{2}{3}}\right]} \tag{6}$$

Where Φ represents the porosity of each nanoscale pore diameter interval, %; r represents average pore size, μm; τ represents the tortuosity. Noted that the tortuosity was obtained from Plessis's empirical formula [60,61]; K_1 represents the permeability of ultra-micropore, micropore and mesopore, mD; K_2 represents the permeability of macropore, mD.

From Fig. 14, it can be seen that the permeability evolution of the nanoscale pore diameter interval in various rank coals. As the pore size increases, the permeability of the coal increases progressively, which can be divided into four stages according to the type of pore. Although the permeability has increased by orders of magnitude from ultra-microporous to microporous and mesoporous (from stage I to stage II

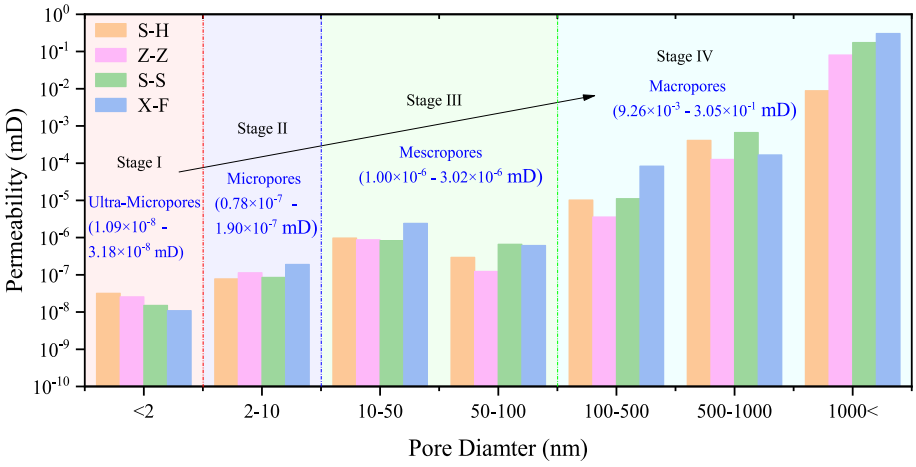

Fig. 14. Distribution of permeability in various pore size segments.

and stage III), it only accounts for less than 1% of the total permeability. In contrast, the permeability is mainly provided by macropores (stage IV), which account for about 99% of the total permeability. The reason may be the large volume covered by macropores, which can connect other independent pores to form a new pore network system, improving the seepage capacity of coal reservoirs. Although, ultra-micropores are well developed in coal (Fig. 9), most of them are isolated pores with poor connectivity, which results in the inability of the gas to migrate. In addition, it was observed that the total permeability gradually decreases from low-rank coal to median-and high-rank coal. They were calculated by Eqs (4) and (5), with 9.26×10^{-3} mD, 8.05×10^{-2} mD, 1.74×10^{-1} mD and 3.05×10^{-1} mD, respectively. This phenomenon is caused by physical compaction and cementation, which leads to a significant reduction in the number of macropores, weakening the permeability of the coal during coalification [25,37]. Moreover, macropores are developed and porosity is relatively high in low-rank coal (Figs. 8 and 12), so the permeability of low-rank coals is greater than other rank coals. In addition, it should be noted that the calculated permeability values are different from the experimental values [35,39,62–64]. The main reasons are as follows: (1) the experimental permeability values were measured under confining pressure, which caused partial pore collapse or closure, resulting in a lower experimental value; (2) although the tortuosity was applied to calculated permeability values under the idealized capillary bundles, the pore structure in coal reservoir is complex; (3) the calculated values represent the seepage capacity of all pores, while the experimental values only represent the seepage capacity of interconnected pores in the coal reservoir. Based on the above discussion, we can know that the permeability is mainly provided by macropores and the development of micropores, mesopores and macropores in low-rank coals is better than in medium-and high-rank coals (Fig. 9). Therefore, it can be concluded that low-rank coals have better connectivity than medium- and high-rank coals. This is because the large pores can connect more small pores, forming a new pore network model that greatly improves the connectivity of the pores in the coal. However, as the maturity of the coal grows, large pores in the coal are filled or collapsed, resulting in a reduction in the number of large pores and a significant increase in the number of small pores. Simultaneously, the falling off of aliphatic structures and the condensation of aromatic structures in the coal macromolecular structure are also main factors in the reduction of large pores and the increase of small pores. Therefore, the connectivity of the nanopores in the coal will gradually weaken during coalification.

5. Conclusion

Based on the combined method of CO_2/N_2 adsorption and synchrotron radiation Nano-CT experiment, the following conclusions about full-scale pore structure characterization during coalification can be obtained:

1. The 3D pore network model of coal was reconstructed by synchrotron radiation Nano-CT experimental. Furthermore, with increasing maturity, the number of pores is gradually reduced, and the effective diameter is less than 0.5 μm, accounting for 97.4%–99.6% of the total number of macropores.
2. A combination of these methods, including CO_2/N_2 adsorption and Nano-CT, accurately characterize the multi-scale pore distribution in coal, ranging from <2 nm, 2–300 nm and 64 nm - 3.5 μm, respectively. The ultra-micropores in various rank coals occupy the primary advantage, accounting for approximately 60.3%–95.2% of the pore volume and the micropores, mesopores and macropores are poorly developed in coal, accounting for approximately 0.7%–9.7%, 1.7%–9.9% and 1.3%–20.2%, respectively.
3. As the maturity of the coal grows, the proportion of porosity contributed by ultra-micropores to the total porosity gradually increases, with the contribution increasing by 57.9%. In contrary, the proportion of porosity contributed by micropores, mesopores and macropores to the total porosity gradually decreases, with the contribution decreasing by 81.0%, 82.8% and 93.6%, respectively.
4. The total permeability gradually decreases from low-rank coal to median-and high-rank coal, with 9.26×10^{-3} mD, 8.05×10^{-2} mD, 1.74×10^{-1} mD and 3.05×10^{-1} mD, respectively, which is negatively correlated with coal maturity during coalification. And the total permeability is mainly provided by macropores, which account for about 99% of the total permeability.

CRediT authorship contribution statement

Zhen Shen: Writing – original draft, Visualization, Validation, Investigation, Data curation. **Zhaoping Meng:** Writing – review & editing, Visualization, Resources, Funding acquisition, Formal analysis. **Yu Liu:** Writing – review & editing, Investigation, Conceptualization. **Junhuan Lei:** Writing – review & editing, Visualization. **Weijun Shen:** Writing – review & editing, Visualization. **Huaxin Ren:** Writing – review & editing, Investigation. **Tengwei Gao:** Writing – review & editing, Investigation. **Kun Zhang:** Writing – review & editing, Visualization, Investigation. **Yuheng Wang:** Writing – review & editing, Investigation. **Libo Tan:** Writing – review & editing, Investigation.

Declaration of competing interest

The authors declare that they have no known competing financial interests or personal relationships that could have appeared to influence the work reported in this paper.

Data availability

No data was used for the research described in the article.

Acknowledgments

This work was financially supported by the National Natural Science Foundation of China (Grant No. 42172190), the Beijing Natural Science Foundation (Grant No. 8222071) and the Shanxi Province Science and Technology Major Project (Grant No. 20201102001, 20191102001 and 20181101013). The authors thank the reviewers and the editor for their constructive comments.

References

[1] T.A. Moore, Coalbed methane: a review, Int. J. Coal Geol. 101 (2012) 36–81.
[2] D.K. Mishra, S.K. Samad, A.K. Varma, V.A. Mendhe, Pore geometrical complexity and fractal facets of Permian shales and coals from Auranga Basin, Jharkhand, India, J. Nat. Gas Sci. Eng. 52 (2018) 25–43.
[3] L. Qin, P. Wang, H.F. Lin, S.G. Li, B. Zhou, Y. Bai, D.J. Yan, C. Ma, Quantitative characterization of the pore volume fractal dimensions for three kinds of liquid nitrogen frozen coal and its enlightenment to coalbed methane exploitation, Energy 263 (2023), 125741.
[4] T.T. Guan, J.H. Zhao, G.L. Zhang, D.D. Zhang, B.X. Han, N. Tang, J.L. Wang, K. X. Li, Insight into controllability and predictability of pore structures in pitch-based activated carbons, Microporous Mesoporous Mater. 271 (2018) 118–127.
[5] Y. Liu, C.H. Zhang, Y. Zhang, Evolution mechanism of methane adsorption capacity in vitrinite-rich during coalification, J. Nat. Gas Sci. Eng. 96 (2021), 104307.
[6] Z.P. Meng, S.S. Liu, G.Q. Li, Adsorption capacity, adsorption potential and surface free energy of different structure high rank coals, J. Petrol. Sci. Eng. 146 (2016) 856–865.
[7] C.R. Clarkson, R.M. Bustin, Binary gas adsorption/desorption isotherms: effect of moisture and coal composition upon carbon dioxide selectivity over methane, Int. J. Coal Geol. 42 (4) (2000) 241–271.
[8] A.M.M. Bustin, R.M. Bustin, Total gas-in-place, gas composition and reservoir properties of coal of the Mannville coal measures, Central Alberta, Int. J. Coal Geol. 153 (2016) 127–143.
[9] J.Q. Shi, S. Durucan, I.C. Sinka, Key parameters controlling coalbed methane cavity well performance, Int. J. Coal Geol. 49 (2002) 19–31.
[10] J.C. Pashin, M.R. McIntyre, Temperature-pressure conditions in coalbed methane reservoirs of the Black Warrior basin: implications for carbon sequestration and enhanced coalbed methane recovery, Int. J. Coal Geol. 54 (2003) 167–183.
[11] M. Pillalamarry, S. Harpalani, S.M. Liu, Gas diffusion behavior of coal and its impact on production from coalbed methane reservoirs, Int. J. Coal Geol. 86 (2011) 342–348.

[12] Y.C. Tan, W.J. Hu, J. Cheng, H. Zhao, Y.Y. Du, H.L. Yao, Pt@SAPO-11 bifunctional catalysts with spatial architecture constructed via a seed-directed solvent-free strategy for n-dodecane hydroisomerization, Microporous Mesoporous Mater. 330 (2022), 111607.
[13] Z.P. Meng, J.W. Yan, G.Q. Li, Controls on gas content and carbon isotopic abundance of methane in Qinnan-East coal bed methane block, Qinshui Basin, China, Energy Fuels 31 (2017) 1502–1511.
[14] S. Hou, X. Wang, X. Wang, Y. Yuan, S. Pan, X. Wang, Pore structure characterization of low volatile bituminous coals with different particle size and tectonic deformation using low pressure gas adsorption, Int. J. Coal Geol. 183 (2017) 1–13.
[15] P. Liu, B.S. Nie, Z.D. Zhao, Y.L. Zhao, Q.G. Li, Characterization of ultrasonic induced damage on multi-scale pore/fracture in coal using gas sorption and μ-CT 3D reconstruction, Fuel 332 (2023), 126178.
[16] C.R. Clarkson, N. Solano, R.M. Bustin, A.M.M. Bustin, G.R.L. Chalmers, et al., Pore structure characterization of North American shale gas reservoirs using USANS/SANS, gas adsorption mercury intrusion, Fuel 103 (2013) 606–616.
[17] C. Peng, C. Zou, Y. Yang, G. Zhang, W. Wang, Fractal analysis of high rank coal from southeast Qinshui basin by using gas adsorption and mercury porosimetry, J. Petrol. Sci. Eng. 156 (2017) 235–249.
[18] L.S. Rijfkogel, B. Ghanbarian, Q. Hu, H. Liu, Clarifying pore diameter, pore width, and their relationship through pressure measurements: a critical study, Mar. Petrol. Geol. 107 (2019) 142–148.
[19] J.W. Yan, Z.P. Meng, K. Zhang, H.F. Yao, H.J. Hao, Pore distribution characteristics of various rank coals matrix and their influences on gas adsorption, J. Petrol. Sci. Eng. 189 (2020), 107041.
[20] W. Liu, G. Wang, D.Y. Han, H. Xu, X.Y. Chu, Accurate characterization of coal pore and fissure structure based on CT 3D reconstruction and NMR, J. Nat. Gas Sci. Eng. 96 (2021), 104242.
[21] Z. Li, G.H. Ni, Y. Wang, H.H. Jiang, Y.Z. Wen, H.R. Dou, M. Jing, Semi-homogeneous model of coal based on 3D reconstruction of CT images and its seepage-deformation characteristics, Energy 259 (2022), 125044.
[22] L.L. Sun, C. Zhang, G. Wang, Q.M. Huang, Q.L. Shi, Research on the evolution of pore and fracture structures during spontaneous combustion of coal based on CT 3D reconstruction, Energy 260 (2022), 125033.
[23] Y.X. Zhao, Y.F. Sun, S.M. Liu, Z.W. Chen, L. Yuan, Pore structure characterization of coal by synchrotron radiation Nano-CT, Fuel 215 (2018) 102–110.
[24] X.H. Shi, J.N. Pan, Q.L. Hou, Y. Jin, Z.Z. Wang, Q.H. Niu, M. Li, Micrometer-scale fractures in coal related to coal rank based on micro-CT scanning and fractal theory, Fuel 121 (2018) 162–172.
[25] J. Chen, W. Cheng, G. Wang, Simulation of the meso-macro-scale fracture network development law of coal water injection based on a SEM reconstruction fracture COHESIVE model, Fuel 287 (2021), 119475.
[26] Y. Chen, D. Tang, H. Xu, S. Tao, S. Li, G. Yang, J. Yu, Pore and fracture characteristics of different rank coals in the eastern margin of the Ordos Basin, China, J. Nat. Gas Sci. Eng. 26 (2015) 1264–1277.
[27] J. Pan, Y. Zhao, Q. Hou, Y. Jin, Nanoscale pores in coal related to coal rank and deformation structures, Transport Porous Media 107 (2) (2015) 543–554.
[28] H. Xu, W. Zhou, R. Zhang, S.M. Liu, Q.M. Zhou, Characterizations of pore, mineral and petrographic properties of marine shale using multiple techniques and their implications on gas storage capability for Sichuan Longmaxi gas shale field in China, Fuel 241 (2019) 360–371.
[29] X.L. Wang, D. Zhang, S. Erlei, Z.G. Jiang, C.Y. Wang, Y.P. Chu, C. Ye, Pore structure and diffusion characteristics of intact and tectonic coals: implications for selection of CO_2 geological sequestration site, J. Nat. Gas Sci. Eng. 81 (2020), 103388.
[30] T. Islamoglu, K.B. Idrees, F.A. Son, Z.J. Chen, S.J. Lee, P. Li, O.K. Farha, Are you using the right probe molecules for assessing the textural properties of metal-organic frameworks, J. Mater. Chem. A 10 (2022) 157–173.
[31] S. Brunauer, P.H. Emmett, E. Teller, Adsorption of gases in multimolecular layers, J. Am. Chem. Soc. 60 (2) (1938) 309–319.
[32] E.P. Barrett, L.G. Joyner, P.P. Halenda, The determination of pore volume and area distributions in porous substances. I. Computations from nitrogen isotherms, J. Am. Chem. Soc. 73 (1) (1951) 373–380.
[33] R.M. Bustin, C.R. Clarkson, Geological controls on coalbed methane reservoir capacity and gas content, Int. J. Coal Geol. 38 (1–2) (1998) 3–26.
[34] V.M. Sermoud, G.D. Barbosa, N.S. Vernin, A.G. Barreto Jr., F.W. Tavares, The impact of the adsorbent energy heterogeneities by multidimensional-multicomponent PC-SAFT-DFT, Fluid Phase Equil. 562 (2022), 113546.
[35] Y. Meng, S.M. Liu, Z.P. Li, Experimental study on sorption induced strain and permeability evolutions and their implications in the anthracite coalbed methane production, J. Petrol. Sci. Eng. 164 (2018) 515–522.
[36] P.C. Carman, Fluid flow through granular beds, Trans. Inst. Chem. Eng. 15 (1937) 150–166.
[37] J.H. Li, B.B. Li, Z.H. Wang, C.H. Ren, K. Yang, Z. Gao, A permeability model for anisotropic coal masses under different stress conditions, J. Petrol. Sci. Eng. 198 (2021), 108197.
[38] Z.Z. Wang, Z. Deng, X.H. Fu, G.F. Li, J.N. Pan, M. Hao, H. Zhou, Effects of methane saturation and nitrogen pressure on N_2–enhanced coalbed methane desorption strain characteristics of medium-rank coal, Nat. Resour. Res. 30 (2021) 1527–1545.
[39] Q.Y. Gou, S. Xu, F. Hao, F. Yang, B.Q. Zhang, Z.G. Shu, et al., Full-scale pores and micro-fractures characterization using FE-SEM, gas adsorption, nano-CT and micro-CT: a case study of the Silurian Longmaxi Formation shale in the Fuling area, Sichuan Basin, China, Fuel 253 (2019) 167–179.
[40] Q. Yuan, K. Zhang, Y. Hong, W. Huang, K. Gao, Z. Wang, et al., A 30 nm-resolution hard X-ray microscope with X-ray fluorescence mapping capability at BSRF, J. Synchrotron Radiat. 19 (2012) 1021–1028.
[41] A. Videla, C.L. Lin, J.D. Miller, Watershed functions applied to a 3D image segmentation problem for the analysis of packed particle beds, Part. Part. Syst. Char. 23 (2010) 237–245.
[42] A. Bera, S. Shah, A review on modern imaging techniques for characterization of nanoporous unconventional reservoirs: challenges and prospects, Mar. Petrol. Geol. 133 (2021), 105287.
[43] H. Zheng, F. Yang, Q.L. Guo, S.Q. Pan, S. Jiang, H. Wang, Multi-scale pore structure, pore network and pore connectivity of tight shale oil reservoir from Triassic Yanchang Formation, Ordos Basin, J. Petrol. Sci. Eng. 212 (2022), 110283.
[44] K.S.W. Sing, IUPAC Recommendations 1984: reporting physisorption data for gas/solid systems with special reference to the determination of surface area and porosity, Pore Appl. Chem. (1985) 603–619.
[45] K. Ramesh, K.S. Reddy, I. Rashmi, A.K. Biswas, Porosity distribution, surface area, and morphology of synthetic potassium zeolites: a SEM and N_2 adsorption study, Commun. Soil Sci. Plant Anal. 5 (2014) 2171–2181.
[46] B. Nie, X. Liu, L. Yang, J. Meng, X. Li, Pore structure characterization of different rank coals using gas adsorption and scanning electron microscopy, Fuel 158 (2015) 908–917.
[50] J. Rouquerol, D. Avnir, W. Fairbridge, D.H. Everett, J.H. Haynes, N. Pernicone, J.D. F. Ramsay, K.S.W. Sing, K.K. Unger, Recommendations for the characterization of porous solids (Technical Report), Pure Appl. Chem. 66 (8) (1994) 1739–1758.
[51] K. Zhang, Z.P. Meng, S.M. Liu, H.J. Hao, T. Chen, Laboratory investigation on pore characteristics of coals with consideration of various tectonic deformations, J. Nat. Gas Sci. Eng. 91 (2021), 103960.
[52] Y.B. Lin, Y. Qin, J.W. Qiao, G. Li, H. Zhang, Effect of coalification and maceration on pore differential development characteristics of high-volatile bituminous coal, Fuel 318 (2022), 123634.
[53] Y. Meng, Z.P. Li, F.P. Lai, Experimental study on porosity and permeability of anthracite coal under different stresses, J. Petrol. Sci. Eng. 133 (2015) 810–817.
[54] G.N. Okolo, R.C. Everson, H.W.J.P. Neomagus, M.J. Roberts, R. Sakurovs, Comparing the porosity and surface areas of coal as measured by gas adsorption, mercury intrusion and SAXS techniques, Fuel 141 (2015) 293–304.
[55] M. Mastalerz, A. Schimmelmann, A. Drobniak, Y. Chen, Porosity of devonian and mississippian new albany shale across a maturation gradient: insights from organic petrology, gas adsorption, and mercury intrusion, AAPG Bull. 97 (10) (2013) 1621–1643.
[56] B. Tsyntsarski, B. Petrova, T. Budinova, N. Petrov, L.F. Velasco, J.B. Parra, C. O. Ania, Porosity development during steam activation of carbon foams from chemically modified pitch, Microporous Mesoporous Mater. 154 (2012) 56–61.
[57] J.Y. Wang, F.J. Jiang, Q.H. Hu, C.L. Zhang, X.G. Yang, W.L. Mo, X.R. Wang, Z. G. Qi, A quantitative model and controlling factors of secondary pore development for tight sandstone reservoirs in the carboniferous Benxi Formation, Ordos Basin, China, Mar. Petrol. Geol. 148 (2023), 106034.
[58] Y. Liu, Y.M. Zhu, W. Li, J.H. Xiang, Y. Wang, J.H. Li, Molecular simulation of methane adsorption in shale based on Grand Canonical Monte Carlo method and pore size distribution, J. Nat. Gas Sci. Eng. 30 (2016) 119–126.
[59] W.J. Shen, L. Zuo, T.R. Ma, C. Chen, C.Z. Qin, L. Yang, K. Xie, Quantitative studies on the characterization and evaluation of adsorbed gas and free gas in deep shale reservoirs, Energy Fuel. 37 (5) (2023) 3752–3759.
[60] X.H. Shi, J.N. Pan, L.L. Pang, R. Wang, G.F. Li, J.J. Tian, H.C. Wang, 3D microfracture network and seepage characteristics of low-volatility bituminous coal based on nano-CT, J. Nat. Gas Sci. Eng. 83 (2020), 103556.
[61] P. Xu, B.M. Yu, Developing a new form of permeability and Kozeny–Carman constant for homogeneous porous media by means of fractal geometry, Adv. Water Resour. 31 (2008) 74–81.
[62] Y. Meng, Z.P. Li, Experimental comparisons of gas adsorption, sorption induced strain, diffusivity and permeability for low and high rank coals, Fuel 234 (2018) 914–923.
[63] Z.Z. Wang, J.N. Pan, Q.L. Hou, Q.H. Niu, J.J. Tian, H.C. Wang, X.H. Fu, Changes in the anisotropic permeability of low-rank coal under varying effective stress in Fukang mining area, China, Fuel 234 (2018) 1481–1497.
[64] Y.F. Sun, Y.X. Zhao, L. Yuan, Quantifying nano-pore heterogeneity and anisotropy in gas shale by synchrotron radiation nano-CT, Microporous Mesoporous Mater. 258 (2018) 8–16.